Neuro-Hotnet: A Graph Theoretic Approach for Brain FC Estimation

Nathan Tung^a, Eli Upfal^a, Jerome Sanes^{b,c}, and Ani Eloyan^{d,*}

^aDepartment of Computer Science, Brown University, Providence, RI 02912
^bDepartment of Neuroscience and Carny Institute for Brain Science, Brown University, Providence, RI 02912

^cCenter for Neurorestoration and Neurotechnology, Providence VA Medical Center, Providence, RI 02908

^dDepartment of Biostatistics, Brown University, Providence, RI 02903 *Corresponding author: ani_eloyan@brown.edu

Abstract

There has been increasing interest in the potential of multi-modal imaging to obtain more robust estimates of Functional Connectivity (FC) in high-dimensional settings. We develop novel algorithms adapting graphical methods incorporating diffusion tensor imaging (DTI) and statistically rigorous control to FC estimation with computational efficiency and scalability. Our proposed algorithm leverages a graphical random walk on DTI data to define a new measure of structural influence that highlights connected components of interest. We then test for minimum subnetwork size and find the subnetwork topology using permutation testing before the discovered components are tested for significance. Extensive simulations demonstrate that our method has comparable power to other currently used methods, with the advantage of greater speed, equal or more robustness, and simple implementation. To verify our approach, we analyze task-based fMRI data obtained from the Human Connectome Project database, which reveal novel insights into brain interactions during performance of a motor task. We expect that the transparency and flexibility of our approach will prove valuable as further understanding of the structure-function relationship informs the future of network estimation. Scalability will also only become more important as neurological data become more granular and grow in dimension.

Keywords: algorithms, graphical models, diffusion kernels, functional brain networks, task-based functional connectivity.

1 Introduction

Brain functional connectivity (FC) is the field of study concerned with the estimation of functional connections between brain regions. Functional magnetic resonance imaging (fMRI) has been widely used in the past few decades for quantifying FC (Lindquist et al. (2008), Penny et al. (2011), Ashby (2019)). In a typical FC study, one has a pre-defined set of seed regions often selected based on anatomical considerations. Each seed region typically comprises a collection of neighboring voxels or individual voxels. Next, one averages the blood-oxygen-level-dependent (BOLD) fMRI intensities in each region across space for each time point and obtains a time series $Y_{ir}(1), \ldots, Y_{ir}(T)$, for participant $i = 1, \ldots, I$, in region $r = 1, \ldots, R$, assuming the number of participants in the study is I, the number of regions of interest (ROIs) is R, and data are collected at T time points. A simple approach for obtaining a brain FC map is based on computing the Pearson correlation between each pair of regions. As a result, one obtains an $R \times R$ matrix of correlations defined by C_i for participant $i = 1, \ldots, I$.

Graph theory (Chung (2019), Bullmore and Bassett (2011)) is commonly used for analyzing brain FC. In this context, one considers each region of interest as a vertex in an undirected graph defined as $G_R = (V, E)$, where V represents the vertices of the graph and E represents the edges. One may consider a weighted graph where the correlation between each pair of regions is the weight on the edge connecting vertices corresponding to the regions. Computationally efficient approaches for estimation of such graphs have been proposed, such as by estimating the precision matrix of fMRI time courses. However, many of these approaches may not be scalable to very large values of R. Gaussian graphical models have been implemented for estimating FC by incorporating structural connectivity (SC) via a prior distribution (Higgins et al., 2018).

Accurate detection of subnetworks in the FC graph is imperative for correct network level inference. Estimation of population-level FC has been considered to compare FC between populations of interest and to use population FC maps for better estimation of subject-level FC. For example, Caffo et al. (2010) proposed an approach for estimation of population FC by applying the singular value decomposition in two-stages to reduce the dimension of fMRI data and then investigated associations of the resulting FC estimates and cognitive impairment in Alzheimer's disease. We propose a novel biologically motivated and computationally efficient approach for estimation of the FC graph in high dimensions. Our proposed approach aims to estimate FC at both the subject- and the population-levels. To scale up the FC estimation approach to high dimensions, we leverage biological prior assumptions on the connection between FC and SC. To accomplish this goal, we extend and implement a heat diffusion approach named HotNet proposed by Vandin et al. (2011) for analyzing graphs in the setting of genomic data analysis. Implementation of the HotNet approach requires the existence of a prior SC map. Hence, we provide a brief overview of diffusion tensor imaging (DTI)-based SC estimation and use DTI-based SC maps when estimating FC.

Our proposed approach is based on using ideas from heat diffusion (Kondor and Lafferty (2002), Lafferty and Lebanon (2005)) to estimate and incorporate the local topology of the SC graph when estimating the FC and performing inference using FC. Qi et al. (2008) proposed a diffusion kernel-based method for analyzing genetic interactions in yeast. Ma et al. (2007) used heat diffusion to develop an approach for prioritizing genes using a combination of gene expression and protein-protein interaction networks. We test two methods using our proposed novel notion of incorporating SC, one building off a recent approach to FC estimation known as structurally informed Gaussian graphical model (siGGM, Higgins et al. (2018)) and the other a simpler, more scalable model. We will refer to our new treatment of siGGM as "siGGM with Diffusion" and our newly developed scalable model as "Neuro-Hotnet". We found that both methods are more robust to noise than existing approaches and identify components expected to have involvement in motor tasks, such as those containing the motor cortex and sensory-touch regions that surprisingly do not emerge with prior methods.

2 Materials and Methods

2.1 Data

We modeled the task-fMRI data publicly available by the Human Connectome Project (HCP) at www.humanconnectome.org. Specifically, we used the database of healthy adult participants performing one of several motor tasks. Given a visual cue, the participants were asked to perform one of five tasks: tap left/right fingers, squeeze left/right toes, or move their tongue. Each block of the tasks follows a 3 sec cue and lasts for 12 sec. Each participant performed the experiment during 2 runs each consisting of 13 blocks. The acquisition used a repetition time of 0.72 sec. The task is motivated by Yeo et al. (2011) and Buckner et al. (2011). While the HCP implementation of the task is thoroughly described by Barch et al. (2013), we provide a brief summary of data acquisition details. The whole-brain EPI images were acquired on a 3T Siemens Skyra machine with a flip angle at 52 degrees, BW = 2290 Hz/Px, collecting 72 slices with 2.0mm isotropic voxels, in-plane FOV = 208 × 180mm. In the motor-task, 284 frames per run were acquired.

2.2 Neuro-Hotnet

We propose a modeling approach for task FC following a graph theoretic framework. In this section, we present our proposed Neuro-Hotnet approach by first describing the incorporation of SC using heat diffusion and then showing the selection of connected subnetworks using a two-stage hypothesis testing procedure.

2.2.1 DTI-Based Structural Connectivity

DTI is a widely used MRI technique where the structure of biological tissues in the brain is characterized using anisotropy, magnitude, and anisotropic orientation of water diffusion (Basser et al., 1994). DTI has been used in recent years to obtain SC by tracing the white matter fiber tracts (Mori and Van Zijl, 2002). An example of white matter fiber

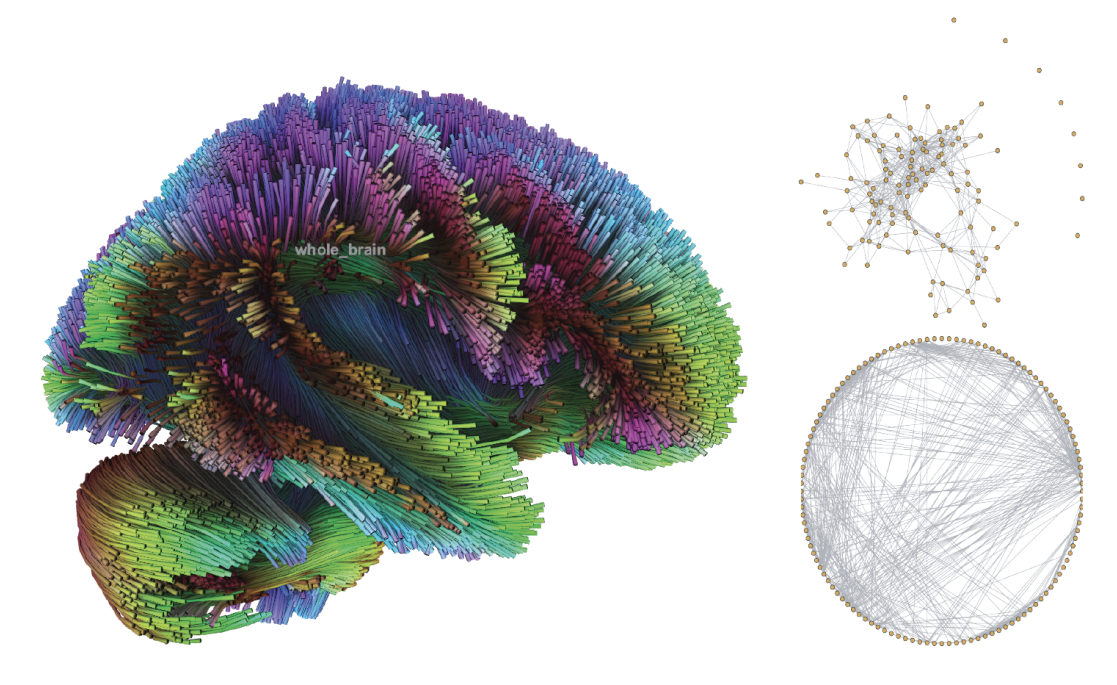


Figure 1: Left: white matter fiber tracts estimated using the HCP template DTI plotted in MNI space. Right: SC graph estimated using the AAL parcellation of a participant specific DTI scan. The graph is presented using a random node structure (top) and a nodes on a circle structure (bottom).

tracts computed using the HCP template DTI dataset is shown in Figure 1. For a given parcellation of the brain, SC between any two pairs of regions can be computed using the number of fiber tracts connecting the regions. Other approaches may be implemented to compute SC incorporating the number of fiber tracts connecting the regions along with the tract lengths (Chung, 2019). Assuming the parcellation includes R regions, we obtain an $R \times R$ matrix for a participant corresponding to their SC. Figure 1 shows the SC graphs computed by using the AAL parcellation of the HCP template DTI dataset, where only the strongest connections (highest number of tracts) are shown.

2.2.2 Heat Diffusion

In the first step of the algorithm to develop Neuro-Hotnet, we obtained a "heat" diffusion process based on the assumption that the strength of interactions between two nodes depends on the neighborhood topology of these nodes. Let $G_n = (V, E)$ denote

the graph corresponding to the structural brain map with edge and node sets E and V respectively, |V| = n. The process of obtaining the SC map can be executed using unweighted (binarized) edges, showing whether there is a large enough number of tracts between two nodes to conclude they are structurally connected, or edges weighted by the number of tracts between all pairs of nodes. The unweighted graph scheme mirrors that proposed by Vandin et al. (2011). However, a weighted approach is incorporated here to take advantage of the additional information on number of tracts between any two ROIs available from DTI. We normalize (Qi et al., 2008) the resulting DTI SC estimate as follows.

$$M' = D^{-1/2}MD^{-1/2}.$$

where M is the matrix representation of the graph G_n and D is the diagonal matrix of row sums of M. For the unweighted graph these are the adjacency matrix and diagonal degree matrix, while for the weighted graph these can simply be thought of as weighted analogs. The elements of the adjacency matrix in both cases are transformed as follows.

$$M'_{ij} = \frac{M_{ij}}{\sqrt{\left(\sum_{m} M_{mi}\right)\left(\sum_{m} M_{mj}\right)}}\tag{1}$$

This process is analogous to scaling the values by node degrees (either the typical or weighted notion) with the result that every path is weighted according to degrees of all the nodes on the path. Let L denote the Laplacian matrix of G_n defined as L = -M' + D', where D' is the diagonal matrix of row sums of M'. We first compute the influence of each node i on the rest of the nodes in the graph. We consider the process where a certain number of random walkers are placed at node i and they diffuse across the graph at a given rate γ . Let $f^i(t) = (f_1^i(t), \ldots, f_n^i(t))$ denote the distribution of heat among the n nodes. Then the equation describing the dynamics of this process is given as follows (Qi

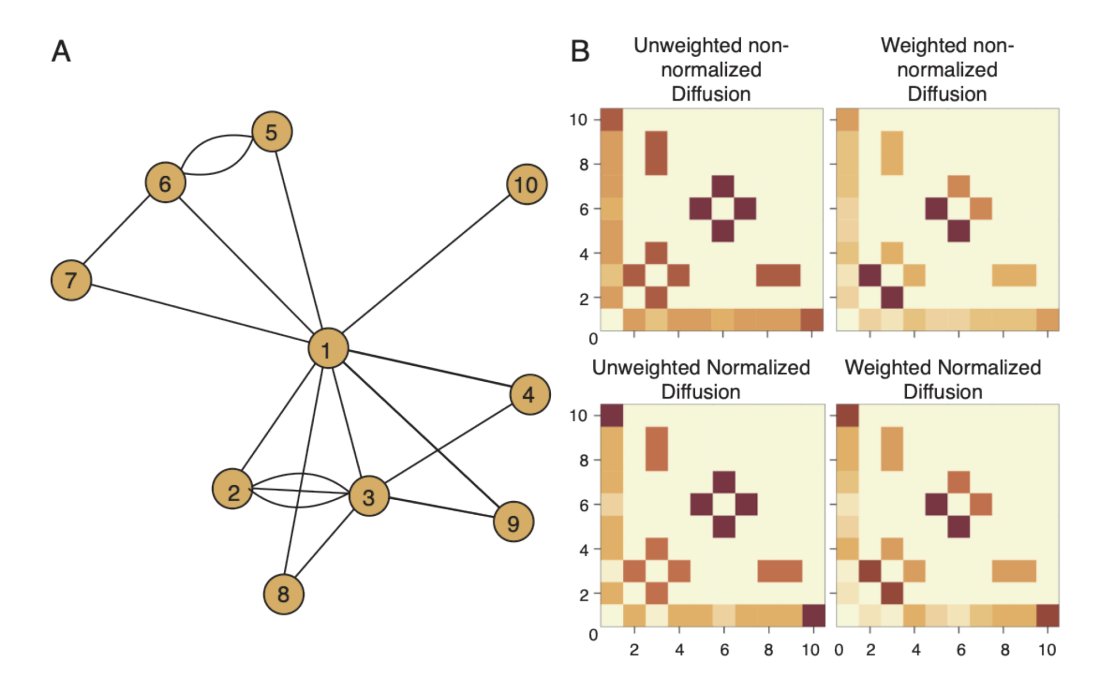


Figure 2: Left: An example undirected graph with 10 nodes. Multiple edges indicates relative weighting. Right: Results of heat kernel diffusion process using four different schemes. Here normalization refers to (3), while the process described in (1) is executed for all depicted heatmaps.

et al. (2008), Vandin et al. (2011)).

$$\frac{\partial f^{i}(t)}{\partial t} = -(L + \gamma I)f^{i}(t) + b^{i}u(t) \tag{2}$$

where b^i is a vector of zeros except for 1 at the i^{th} location and u(t) is the unit step function. As $t \to \infty$, the equilibrium of (2) is given by $f^i = (L + \gamma I)^{-1}b^i$.

The influence of all node pairs may be computed simultaneously as $f = [(L + \gamma I)^{-1}]^T$, where f_{ij} is the influence of node i on node j. After the influence matrix is computed it is once again normalized, as in Higgins et al. (2018), so that each entry i, j can be thought of as the probability that a tract with an endpoint in region i has its other endpoint in region j. Formally, we obtain the influence matrix $G(\gamma)$ such that

$$G(\gamma)_{ij} = \frac{1}{2} \left[\frac{C'_{ij}}{C'_{i*}} + \frac{C'_{ji}}{C'_{j*}} \right], \tag{3}$$

where C'_{i*} and C'_{j*} are the sums of rows i and j, respectively. In practice, this step

functions similarly to the degree-normalizing step before inverting the Laplacian, i.e., reducing influence on high degree nodes.

In Figure 2, the diffusion process is illustrated using a toy example. Influence from node 1 is spread among its many neighbors, whereas the influences between 5, 6, and 7, for example, are strong, since they have relatively few other neighbors. It is clear that weighting the diffusion process appropriately incorporates the relative weights of edges (2-3, 5-6). The dampening effect of node 1's influence due to its many neighbors is more pronounced with the normalizing step (3) than without, as illustrated by the strength of connection on the edge 1-10 in the normalized map as compared to the lower strength of connection between 1 and the rest of its edges. A pseudocode outline of the diffusion scheme implemented for DTI data is illustrated in Algorithm 1.

Algorithm 1 Diffusion Algorithm

```
Input: SC matrix M and flow-rate parameter \gamma

Output: Influence Graph G(\gamma)

1: Construct diagonal node-degree matrix D with D_{ij} = \mathbb{1}_{i=j} \times \sum_{x=1}^{p} M_{ix};

2: M' \leftarrow D^{-1/2}MD^{-1/2};

3: Construct D' with D'_{ij} = \mathbb{1}_{i=j} \times \sum_{x=1}^{p} M'_{ix};

4: L \leftarrow -M' + D' + \gamma I;

5: Linv \leftarrow [L^{-1}]^M;

6: for i \in \{1, \dots, p\} do

7: for j \in \{1, \dots, p\} do

8: G(\gamma)_{ij} = average\left(\frac{Linv_{ij}}{\sum_{x=1}^{p} Linv_{ix}}, \frac{Linv_{ji}}{\sum_{x=1}^{p} Linv_{jx}}\right)

9: end for

10: end for

11: return G(\gamma)
```

The idea behind this approach parallels the following description on social network modeling (Figure 3). Suppose individual D in a social network is connected to a large number of individuals, while individual B is connected to few others in the network. If A is connected to C through D this connection may not be of interest, as D is connected to a lot of individuals implying that many of their connections are superficial: the influence between A and C would become down-weighted. If A is connected to C through B their

connection potentially has more interest as B's few neighbors imply its connections are substantial: the influence between A and C would then become up-weighted. Replacing people in this canonical example with ROIs gives the reasoning behind the diffusion process. In this approach, not only the number of connected components of the two ROI's, but also those of all nodes in the path connecting them are taken into account.

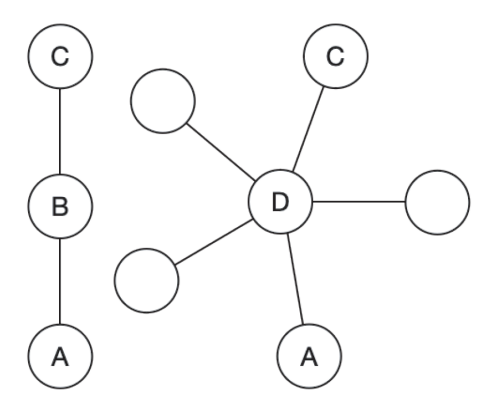


Figure 3: Chain versus star graph.

2.2.3 Incorporating Structural Connectivity

In this subsection, we discuss incorporating SC via heat diffusion when computing the FC graph using a weighted correlation approach. Though, the correlation approach is selected as an example, we will show that SC can be incorporated in computing FC using other approaches. Let $\tilde{Y}_{ir}(t)$ denote the normalized BOLD fMRI response at time $t=1,\ldots,T$ for participant i in region $r=1,\ldots,R$ and \tilde{Y}_i the corresponding $R\times T$ matrix or time courses for participant $i=1,\ldots,n$. Since the influence matrix is symmetric, given that DTI tracts are undirected, we compute the weight of the graph edge connecting a given pair of nodes r_1, r_2 as follows.

$$c_{ir_1r_2}(t) = c_{ir_2r_1}(t) = f_{r_1r_2} \times \tilde{Y}_{ir_1}(t) \cdot \tilde{Y}_{ir_2}(t). \tag{4}$$

Let $\bar{c}_{ir_1r_2}$ define the average weight of the edge of the graph, where the average is computed over time. If \tilde{P}_i denotes the $R \times R$ sample correlation matrix of \tilde{Y}_i^T , then $\bar{c}_{ir_1r_2} = f_{r_1r_2} \times \tilde{P}_{ir_1r_2}$ is equal to the sample correlation weighted by the influence computed based on SC. To determine whether nodes r_1 and r_2 are connected at the population level, we test the following hypotheses for all pairs r_1 and r_2 .

$$H_0: W_{r_1r_2} = 0 \text{ vs } H_a: W_{r_1r_2} \neq 0,$$
 (5)

where W is the $R \times R$ matrix of population-level FC for a given task state ($W_{r_1r_2}$ is the average of $\bar{c}_{ir_1r_2}$ over all participants). Note, if the influence graph weights in (4) are all equal to one and the product function is used to define the function in (4), then the sample correlation \tilde{P}_i alone can be used to estimate the subject-level FC and the hypothesis tests in (5) are equivalent to performing Pearson correlation-based estimation of FC (SC naive approach).

Figure 4 illustrates how the proposed framework combines Pearson correlation used in the SC naive approach with the DTI-based diffusion process to derive a novel notion of influence incorporating both sources. The same example undirected graph G_R as in Figure 2 is presented. Clear examples of the neighborhood topology being taken into account to uncover more interesting discoveries can be seen. A stronger correlation of 0.9 was placed between nodes 1 and 3 and a weaker correlation of 0.7 placed between nodes 1 and 10. Despite this difference the estimated FC places dramatically higher weight between nodes 1 and 10 than 1 and 3 due to the down-weighting caused by many neighbors of node 3 encoded in the heat diffusion matrix. This effect can be seen further in the cluster of nodes 2-3-4 vs nodes 5-6-7. Despite all nodes being given an equal correlation of 0.4, the 5-6-7 cluster overall has higher FC estimates than 2-3-4. The concurrent effect of weighting can be seen in 5-6 being slightly stronger than 6-7 (2 vs 1 edge) and 2-3 being very noticeably stronger than 3-4 (3 vs 1 edge).

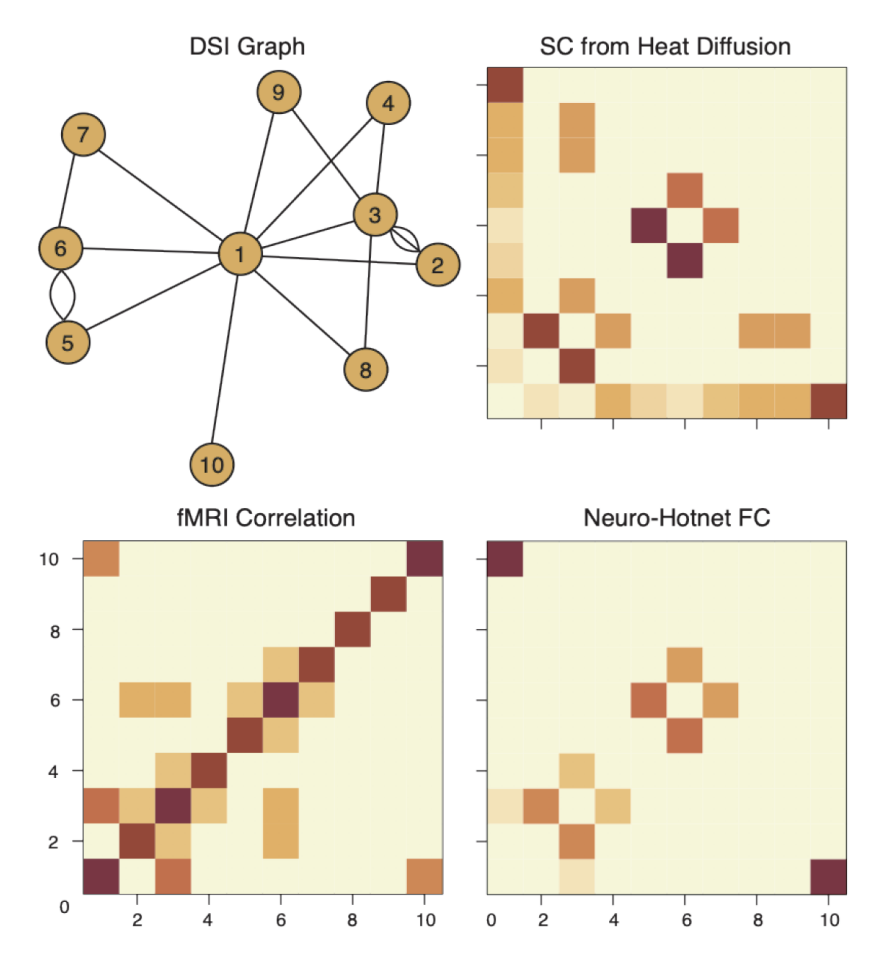


Figure 4: Illustration of computing the heat diffusion matrix (weighted and with normalizing step) and HotNet estimates from a given graph with 10 nodes.

We define the enhanced influence graph $H(\delta)$ to be G_R but with edges below δ removed, i.e. $H(\delta)_{r_1r_2} = W_{r_1r_2} \times \mathbb{1}_{W_{r_1r_2} > \delta}$. To obtain a scalable and robust algorithm for FC estimation, instead of considering individual tests at each pair of nodes as described by the hypothesis tests in (5), we propose performing hypothesis tests to identify subnetworks in the graph $H(\delta)$. Testing for combined hypotheses to evaluate the strength of FC in subnetworks instead of implementing pairwise hypothesis testing procedures is beneficial in some settings (i.e. when the hypothesis tests of interest have patterns of dependence). Multiple comparison corrections that do not take into account these dependencies may not find existing effects.

2.2.4 Hypothesis Testing

We extend the combined hypothesis testing procedure (Efron (2013), Wang and Yuan (2019)) implemented in the context of gene enrichment analysis to estimate significant subnetworks of FC. In gene enrichment analysis, it is often known which gene groups form pathways relating to various functions. Hence, testing for non-null enrichment in each of these pathways, instead of testing for mutations in individual genes is preferred for discovering existing effects that may be missed by individual hypothesis tests even with application of corrections for multiple comparisons. Extending this idea to FC estimation, we propose using the subnetworks of the diffusion enhanced graph as a potential collection of ROI sets that can be functionally connected during the task. Let H_1, \ldots, H_l define the set of all connected components of $H(\delta)$. The size of this collection is 2^R .

In gene enrichment analyses, to reduce the number of simultaneous hypothesis tests for subnetwork discovery, predefined pathways of gene associations are used as groups of genes that are potentially significant as a group even though each individual gene may not be significantly associated with an outcome. The groups of genes within the pathways are tested for significance as a set. In brain FC, such pre-existing pathways are not always available. Instead, we propose a data driven approach for identifying a relatively low number of subnetworks to be tested for significance. First, for each participant in the study given a size of the subnetworks, we test whether there is at least one subnetwork of this size that is significant. We define the probability space $(\Omega, \mathcal{F}, \mathcal{P})$, where Ω is the set of all possible graphs with a connection between a given pair of regions in R, \mathcal{F} is the collection of all possible subnetworks, and \mathcal{P} is the probability measure defined on \mathcal{F} assigning probability of observing any given subnetwork. We assume the Erdos-Renyi model, i.e. the probability of a connection between any two vertices is independent on connections between other vertices in the graph. \mathcal{P} is estimated using the empirical distribution $p(r_1, r_2) = \frac{1}{I} \sum_{i=1}^{I} \mathbb{1}_{W_{r_1 r_2} > \delta}$, where $W_{r_1 r_2}$ are the thresholded edge weights in $H_i(\delta)$. For a given size $s=1,\ldots,R$, let X_s define the set of connected components of size

greater than or equal to s, while $|X_s|$ is the support of the set X_s . Let \tilde{X}_s define the set of connected components of a graph where the number of edges e_{Hi} is equal to that of $H_i(\delta)$ and the edges are randomly assigned, i.e. where $p(r_1, r_2) = \frac{e_{Hi}}{D}$ and $D = {R \choose 2}$. Hence, to test whether the subnetwork topology of the observed graphs is different from that where e_{Hi} edges are randomly distributed on the node pairs, we perform the following hypothesis test.

$$H_0: |\tilde{X}_s| = |X_s| \text{ vs } H_a: |\tilde{X}_s| \neq |X_s|$$

$$\tag{6}$$

By performing the hypotheses in (6) we obtain the smallest s, s^* , such that at least one of the connected components of size s^* or above is statistically significantly different from zero.

We perform a combined hypothesis test for each subnetwork in $H(\delta)$ of size at least s^* , call this set $H_s(\delta)$, to test whether FC of the subnetwork is significantly different from zero. For a given subnetwork H in $H_s(\delta)$, let V_H define the set of nodes in H. By our definition, $\tilde{c}_{r_1r_2}(t)$ denotes the weighted z-score of the activation between regions $r_1, r_2 \in V_H$ such that $\tilde{c}_{r_1r_2}(t) = W_{r_1r_2} + \epsilon_{r_1r_2}$, where $\epsilon_{r_1r_2} \sim N(0, \sigma^2)$ are random noise independent across pairs of ROIs. We are interested in testing the following combined hypothesis

$$H_0: W_{r_1r_2} = 0, \forall r_1, r_2 \in V_H \text{ vs } H_a: W_{r_1r_2} \neq 0, \text{ for some } r_1, r_2 \in V_H$$
 (7)

We test for significance of subnetworks of a given size to reduce the number of simultaneous hypothesis tests following an approach proposed by Vandin et al. (2011). The estimated temporal correlation matrix \tilde{P}_i of participant i represents the FC between each pair of nodes solely based on \tilde{Y}_i without incorporating SC. To implement the hypothesis test presented in (6), we use a permutation testing approach. To obtain the distribution of the test statistic under the null hypothesis conditioned on the number and magnitude of edges derived from \tilde{P}_i , we permute the weighted edges of the connectivity graph uni-

formly at random, or equivalently permute the entries of \tilde{P}_i . When combined with SC in Neuro-Hotnet, we can test for significance to obtain identities of ROIs. Given \tilde{P}_i let \tilde{P}_i^f be a flattened version with dimensions $1 \times R^2$. Given a uniformly random permutation of the set $\{1, \ldots, R^2\}$, defined as R', we compute $\tilde{P}_i^f[R']$ which can then be unflattened back to the $R \times R$ matrix \tilde{P}_i' . This represents the covariance matrix under the null hypothesis, i.e., a uniformly random permutation of the edges of \tilde{P}_i . Given a number of such permutations, we compute the distribution of the test statistic and then calculate the probability of observing the enhanced influence graph using the BOLD signals empirically to obtain a p-value for testing (6).

2.2.5 Testing of Individual Components

The fact that the number of connected components of size at least s^* is statistically significant does not necessarily imply that each of the connected components is significant. To address the possibility of Type II error, Vandin et al. (2011) have added a condition while testing for significance of the number of components of size s that also requires the count for s to be greater than the expected count for s under the null hypothesis such that the resulting test controls the False Discovery Rate (FDR) at a pre-specified value β . Vandin et al. (2011) prove that this scheme controls the FDR at β without the need to test each individual component as doing so was found to be infeasible in the domain of gene pathways. However, in the brain FC domain, testing each connected component individually is more feasible and confers many advantages based on the number of ROIs considered and our extensive experimental results. We explore these advantages in depth through simulations in Section 3. In brief, our proposed approach allows for discovery of smaller components, more precise quantification of significance of each result, and more robust results in extreme cases of agreement or disagreement between Pearson correlation and the influence graph. Such component-specific testing is also quite easily implemented and computationally efficient.

To formalize our proposed approach for testing the individual edges in the resulting significant subnetworks, let H be a set of size s nodes in $H_s(\delta)$ representing a connected component. Let $Z_{ir_1r_2}$ define the z-scores of the sample correlations $\frac{P_{ir_1r_2}}{\tilde{P}_{ir_1r_1}\tilde{P}_{ir_2r_2}}$ computed using the Fisher z-transform. To test whether FC is significantly different from zero for at least one edge in the connected component H we use the following test statistic (Efron, 2013).

$$S(Z_H) = \frac{1}{s} \sum_{i=1}^{I} \sum_{r_1, r_2 \in H} Z_{ir_1 r_2}$$
(8)

We obtain a p-value for each connected component. The pseudocode is given in 2.

Algorithm 2 Neuro-Hotnet Algorithm

Input: Average regional cross-correlation across all N participants \tilde{P} , Influence Graph $G(\gamma)$, and parameters δ, n, K, α

Output: Connected components and their p-values

- 1: $En \leftarrow \tilde{P} \odot G(\gamma)$;
- 2: Replace any values of En below δ with 0
- 3: Create vector $C: C[s] = \sum_{S \in E} \mathbbm{1}_{|S| > = s}, \forall s \in \{1, \dots, K\}$ where E is the set of all connected components of En
- 4: Initialize vector p of p-values to 0
- 5: Initialize vector e of expected counts to 0
- 6: for n times do
- Shuffle \tilde{P} (null distribution), call this \tilde{P}_0
- Repeat steps 1 through 3 with \tilde{P}_0 in place of \tilde{P} , yielding En_0, C_0 under the null
- Update $p[s] \leftarrow p[s] + \frac{\mathbb{I}_{C_0[s] > C[s]}}{n}, \forall s \in \{1, \dots, K\}$ Update $e[s] \leftarrow e[s] + \frac{C_0[s]}{n}, \forall s \in \{1, \dots, K\}$
- 11: end for
- 12: $s^* \leftarrow min\{s : p[s] < \frac{\alpha}{K}\}$
- 13: **for all** $\{c : c \in E \land |c| \ge s\}$ **do**
- Conduct two-sample t-test and store p-value. Sample 1: $average\{\tilde{P}_k[i,j]:i,j\in$ $c\}, \forall k \in \{1, \ldots, N\}.$ Sample 2: $average(\tilde{P}_k), \forall k \in \{1, \ldots, N\}$
- 15: end for
- 16: **return** all $\{c: c \in E \land |c| \ge s\}$ and corresponding p-values

2.3 Gaussian Graphical Models

In this subsection, we discuss incorporating our proposed modeling of the diffusion processes in an example FC estimation approach using Gaussian Graphical modeling. Methods such as siGGM, as proposed by Higgins et al. (2018), that use Bayesian Gaussian graphical models in lieu of multiple hypothesis testing have shown promise in structurally-informed FC estimation. Given $Y_i(t), t = 1, ..., T$, representing the vector of BOLD signals at all ROIs at time t, siGGM assumes the statistical probabilistic model $Y_i(t) \sim N(0, K_i^{-1})$, where K is the inverse covariance matrix. Graphical lasso (Friedman et al., 2008) is a commonly used regularization method for estimation of precision matrices by incorporating sparsity as follows.

$$\hat{K}_i = argmax_{K_i \in M_R^+} \log \det(K_i) - trace(\Sigma_i K_i) - \lambda \sum_{j \le k} |K_{ijk}|$$
(9)

where M_R^+ is the cone of $R \times R$ symmetric positive definite matrices, while Σ_i defines the sample covariance matrix. In the past decade, population level FC estimates have been used to obtain more precise estimates of subject-level covariance. Bayesian graphical models (Wang et al., 2012) are a convenient modeling approach implemented for incorporating population level maps using prior distributions. Higgins et al. (2018) proposed using anatomical knowledge (SC) as a prior for estimation of subject-specific FC using the following prior density for the inverse covariance.

$$P(K_i|\lambda) = Z_{\lambda}^{-1} \prod_{r=1}^{R} Exp(K_{irr}|\lambda) \prod_{j < r} DE(K_{ijr}|\lambda) I(\Sigma_i \in M_R^+)$$

While the prior densities implemented for incorporation of SC are given as follows.

$$P(K_i|\lambda) = Z_{\lambda,\nu}^{-1} \prod_{r=1}^R Exp(K_{irr}|\frac{\nu}{2}) \prod_{j < r} DE(K_{ijr}|\nu\lambda_{jr}) I(\Sigma_i \in M_R^+)$$

$$P(\lambda|\mu,\eta) = Z_{\lambda,\nu} \prod_{j < r} LN(\mu_{jr} - \eta e_{jr}, \sigma_{\lambda}^2)$$

Details of interpretation and choice of prior parameters are presented by Higgins et al. (2018). We propose incorporating the diffusion process outlined above to obtain subject-

specific FC estimates while using our heat diffusion SC within the framework of siGGM. This flexible framework allows for estimation of FC by replacing the SC by the influence graph from the above diffusion process. We assume BOLD fMRI signals are normalized, i.e. using \tilde{Y}_i , to ensure that the observations and SC are on the same scale.

Note that the above approach is aimed at estimation of FC at the subject-level. To obtain a population level estimate of FC given a sample of fMRI scans, we propose the following approach. For each participant's fMRI data, we calculate the sample covariance matrix across regions over all time points. These covariance matrices are then averaged and used as input in siGGM to obtain a population-level FC estimate. Let $C(\nu)$ be the maximum posterior log-likelihood siGGM estimate of the population-level $R \times R$ covariance matrix incorporating all normalized BOLD signals \tilde{Y}_i^T and $G(\gamma)$. ν refers to the tuning parameter controlling the network's overall sparsity and must be tuned to balance number of discoveries with sensitivity. Then we use the set of connected components of $C(\nu)$, that we define by $S(\nu)$, as subnetworks of interest to be tested in the second stage of Neuro-Hotnet as the set of chosen components to test for significance. The rest of the algorithm mirrors Neuro-Hotnet, testing the hypotheses in (7) for each $S \in S(\nu)$. When implementing the siGGM method, we used the source code provided by the authors (see Higgins et al. (2018)) and the default configurations of the parameters to adjust the relative impact of structural influence and observations.

3 Simulations

In this section we first perform a realistic simulation using the parameters estimated from the HCP data to compare the ability of Neuro-Hotnet, siGGM with and without Diffusion, and the SC naive approach to estimate a known FC graph with fMRI data generated with additive noise from a structural prior. Then we compare runtimes of both novel algorithms (Neuro-Hotnet and siGGM with Diffusion) and how they scale with graph size. Finally, the Neuro-Hotnet algorithm is tested in-depth by carrying out several simulations to examine edge cases with regard to the relationship between BOLD fMRI, FC, and SC.

3.1 Comparing and Examining Methods

Study 1: data parameters with noise. To compare the performance of the SC naive approach, raw siGGM (no diffusion), siGGM with Diffusion, and Neuro-Hotnet, we generate sample SC graphs with R = 120, 300, 500 nodes and compare the accuracy of each method in recovering these graphs. For each $r \in \{120, 300, 500\}$, an SC graph M_r is generated with density 0.3 (30% of all pairwise edges are nonzero) and edge weights generated from the uniform(0,1) distribution. For each M_r we generate n = 308 samples from a Gaussian distribution under the assumption that the row means, standard deviations, and dimensions mirror those of the HCP data, but correlations are equal to M_r scaled to the nearest correlation matrix c_{M_r} . With M_r denoting the $r \times r$ symmetric matrix representation of the graph edges,

$$\rho_{M_r} = \frac{M_r}{\max |M_r|},$$

$$\rho_{M_{r_{ij}}} = 1, \forall i, j \in \{1, \dots, r\} \land i = j,$$

$$\Sigma_{M_r} = \text{nearPD}(S \times S^T \odot c_{M_r}),$$
(10)

where Σ_{M_r} is the nearest covariance matrix used to generate the sample. For ease of visualization and comparison and to mimic the results from the HCP analyses, all components of size < 8 were removed before conversion to the nearest correlation matrix. The nearest positive definite matrix for a given matrix A is computed using the method by Higham (2002) that finds the positive semidefinite matrix with unit diagonal minimizing $\{\|A - X\| : X \text{ is a correlation matrix}\}$, where $\|\cdot\|$ is a weighted Froebenius norm. Noise was then similarly generated for each participant from a multivariate Gaussian distribu-

tion with mean 0 and standard deviation 10,000 (roughly the mean signal strength of 9,600) for all regions, all independent of each other. Such a high variance is necessary to introduce sufficient noise due to the large number of participants and the fact that the BOLD fMRI signal noise is somewhat reduced when regional correlation is calculated. This simulation mirrors the structure of the HCP data, because each M_r represents the anatomical brain structure that gives rise to the observations that are then contaminated by noise due to participant differences and measurement error.

Figure 5 shows differences in estimation accuracy over 200 trials for each method for each graph. All SC informed methods perform significantly better than SC naive, reaching over 70% recovery at all sizes at this level of noise despite the low error tolerance (see Figure 5 caption) used to define a successfully estimated component. For both methods utilizing the diffusion process γ was set at 0.01. We obtain that with $\gamma = 0.01$ incorporating the diffusion process results in at least similar recovery accuracy as the methods not utilizing diffusion. In fact, incorporating the diffusion process strictly improves recovery rates for siGGM. siGGM methods perform better than Neuro-Hotnet on the smallest graph, likely due to the assumption in Neuro-Hotnet that smaller components are of less interest. This difference is less significant if one prioritizes larger components (or as graph size increases). In general, there is a drop in recovery rate with increasing number of ROIs, but this drop is slower for SC informed methods. The same thresholds and parameters were used for all sizes and were chosen for fair comparison. For Neuro-Hotnet $\delta = 5.5 \times 10^{-4}$ was used, $\nu = 2.5 \times 10^{-4}$ for raw siGGM, $\nu = 3.5 \times 10^{-4}$ for siGGM with Diffusion, and $\varepsilon=1\times 10^{-3}$ for SC Naive. $\alpha=0.1$ and k=10 were chosen for Neuro-Hotnet.

Study 2: runtimes. We compare execution times of Neuro-Hotnet against those of siGGM with Diffusion across 10 different graph sizes (number of ROIs) to determine how their runtimes may scale with advancements in data collection methods resulting in finer parcellations of the brain and thus higher dimensional graphs. For each graph size, a

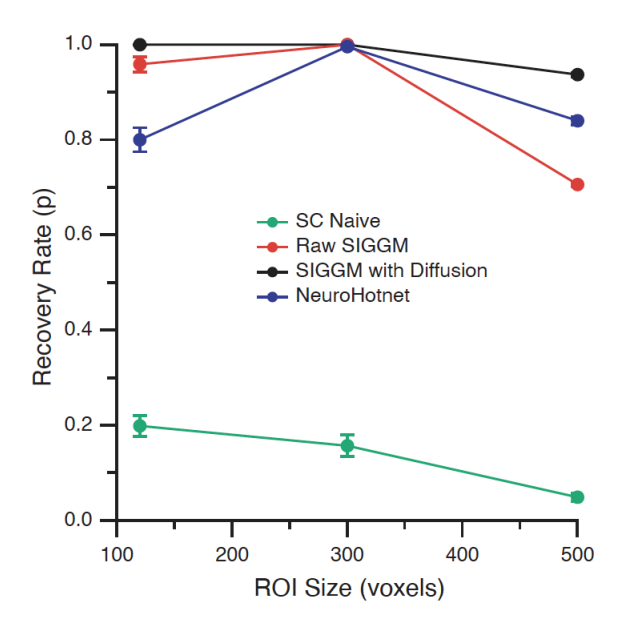


Figure 5: Comparison of each method's average recovery rate for components of randomly generated SC graphs of varying sizes. 200 high-noise trials were run for each graph. Orange error bars represent 95% confidence intervals. Rates for each graph are calculated as the proportion of components in the graph that have a match in a method's estimates, where two components are considered a match if they differ on less than 4 regions (any 3 or less errors, false positives or missing regions, are tolerated).

simulated SC graph is generated as in Study 1 with density 0.3 and uniformly distributed edge weights. Each graph is then used as a prior to generate n=308 participants from a Gaussian distribution just as in Study 1. Both algorithms are then executed 10 times for each graph size on an AMD Ryzen 5 3600 6-Core processor to attain the average runtimes plotted in Figure 6. This illustrates Neuro-Hotnet's superior scalability due to its much simpler model for estimation.

Study 3: data parameters, no noise. We next tested the performance of Neuro-Hotnet when the fMRI data are curated to match the real influence $G(\gamma)$ as above, but with no additive noise. Table 1 shows results for the lowest δ where the first stage of the algorithm returns a significant value of s, namely $s^* = 10$. Even when we choose a 99% confidence interval ($\alpha = 0.01$) the resulting component contains 117 nodes. This is not a very informative outcome and it does not reflect the true underlying structure of the data used for the simulation. Under realistic conditions it is highly improbable to encounter such a large component. The second stage testing of the significance of the

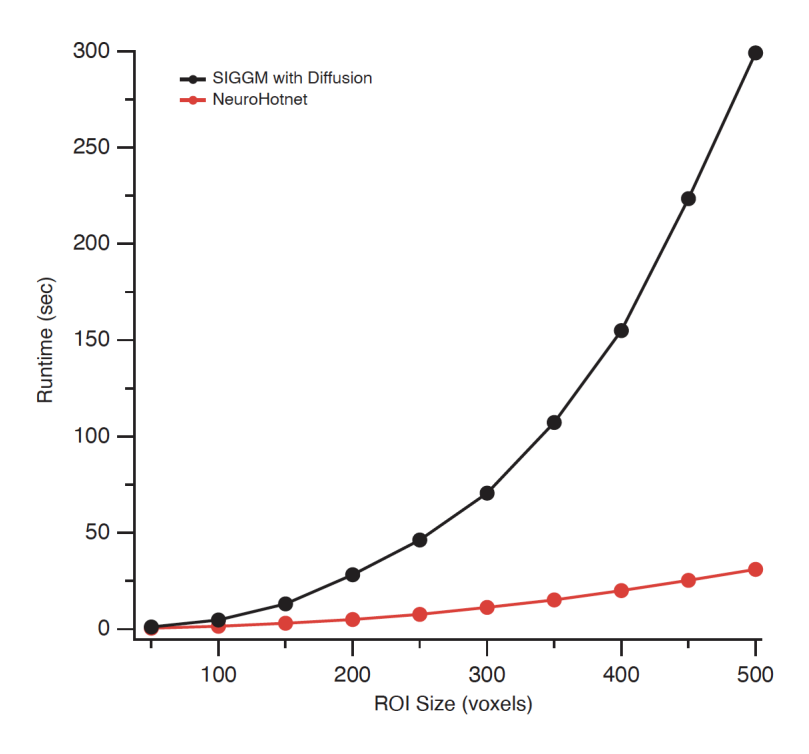


Figure 6: Runtime for both novel algorithms plotted against number of ROIs (i.e. number of nodes in the graph).

specific component rules out this large 117-node discovery, assigning it a high p-value of 0.18. In this domain where it is trivial to individually test the few number of discoveries this novel component-specific test is preferable to the FDR controlling method used in the original Hotnet algorithm developed by Vandin et al. (2011), since our proposed approach was able to exclude the large component that would have been included in the latter FDR condition. Indeed, it is easy to see from Table 1 that the FDR controlling method described in Section 2.2.5 would flag this large component of size 117 (since $\mathbb{E}_{H_0}[X_s] = 0$), resulting in a false positive.

Study 4: Hypothetical fMRI, random $G(\gamma)$. This simulation study was designed to determine whether Neuro-Hotnet, while incorporating $G(\gamma)$, can recover correlations in the fMRI data when $G(\gamma)$ holds no meaningful information. To this end, a hypothetical correlation matrix was constructed that consisted of all 0's except 1's on the diagonal, 0.4 for all edges between rows $1, \ldots, 10$, and 0.6 for all edges between rows $21, \ldots, 50$. fMRI

data for 308 participants were simulated using this matrix as the true correlation map. Edges of $G(\gamma)$ were generated randomly from the uniform(0,0.5) distribution. At $\delta =$ 0.16 both components with nonzero seeded correlations (nodes $1, \ldots, 10$ and $21, \ldots, 50$) are discovered with empirical p-values < 0.0001. As shown in Table 1, expected counts do not decrease as s increases. As a result with the original Hotnet's FDR controlling condition no discoveries would be made, as 2 is not sufficiently larger than 1. The strange behavior of the expected count is due to the large number of edges with correlations concentrated at the highest value (0.6): at low δ a large proportion of these $\binom{30}{2} = 435$ edges are connected under the null hypothesis, i.e. any random distribution of ~ 435 unique edges between 120 nodes is guaranteed to connect at least K=20 nodes (it only takes 190 edges to guarantee 20 connected). In more realistic situations, this combination of extreme stratification of correlation with a large number of edges at the top is highly improbable. But even in this scenario, the individual component testing framework once again allows for the more liberal discovery of these regions and the significant edges are identified (with small p-values). When δ increases to 0.29 the weaker correlated component is removed altogether and the stronger connected component (regions $21, \ldots, 50$) is the sole detected component.

Study 5: fMRI and $G(\gamma)$ Disagree: In this final simulation study, we tested whether there is a reasonable balance of impact between fMRI FC estimated using Pearson correlations and $G(\gamma)$ edges on Neuro-Hotnet's FC estimate. To test the effect of disagreement between fMRI data and the influence graph on the results of Neuro-Hotnet, competing known information is encoded in each of the observations and the influence graph. We used the same hypothetical true correlation matrix and method of simulating observations as in Study 4 in combination with the influence estimated by heat diffusion from HCP DTI data. Table 1 displays the results with threshold $\delta = 0.04$. Since this is a more realistic scenario than Study 4 (influence reflects the true anatomical information and is not purely random), the expected counts do not display the same strange behavior and

	s	Observed X_s	p-value	$\mathbb{E}_{H_0}[X_s]$
	2	1	1.00	13.69
fMRI matches $G(\gamma)$ $\delta = 0.023$	3	1	0.97	3.05
	6	1	0.07	0.07
0 - 0.029	9	1	2×10^{-3}	2×10^{-3}
	10	1	$< 10^{-4}$	0
	2	2	0	1
	5	2	0	1
fMRI from random $G(\gamma)$,	10	2	0	1
$\delta = 0.16$	11	1	1	1
	15	1	1	1
	20	1	1	1
	2	5	1.00	19.69
	4	2	0.90	3.26
Hypothetical fMRI and	8	1	0.20	0.21
random $G(\gamma)$,	10	1	0.05	0.06
$\delta = 0.04$	13	1	8×10^{-3}	8×10^{-3}
	15	1	10^{-3}	10^{-3}
	20	1	10^{-3}	10^{-3}

Table 1: Neuro-Hotnet simulation results. s denotes component size and X_s the number of components of size at least s in the estimated FC matrix. E_{H_0} is expectation under the null hypothesis, while p-values are $P(X_s > E_{H_0}[X_s])$. Rows highlighted in gray denote $s^* =$ the smallest s found statistically significant. Any component of size $\geq s^*$ is marked for individual testing.

decrease with s. In the presence of conflicting information, the algorithm will discover the more distinct results, in this case erring toward the fMRI observations as the correlation seed features harsh jumps between the 0 correlation on most edges and 0.4 and 0.6 for the components. While $G(\gamma)$ certainly contains information, the influences between nodes increase by more natural, smaller increments and thus no components are as starkly distinguished. Because there is conflicting information the algorithm does not detect the weaker correlated regions $1, \ldots, 10$ even at lower thresholds.

4 Results

The SC analysis was performed using the Diffusion MRI Fiber Tracking tool in the DSI Studio software. Using a template image and a DTI diffusion scheme, we obtained

the whole brain SC based on a total of 64 diffusion sampling directions. As a result 23,898 tracts were identified and their coordinates saved in the MNI space. From the resulting set of tracts the SC was obtained from DSI Studio.

4.1 Neuro-Hotnet

To obtain the influence graph, we used the diffusion process with $\gamma=30$, since this was the average node degree in the SC graph. The diffusion process seems robust to this choice since we found the choice of $\gamma=1$ and $\gamma=50$ both result in similar outcomes. The BOLD fMRI response was aggregated across N=308 participants by averaging each participant's sample correlation matrix as $\tilde{P}=\frac{1}{n}\sum_{i=1}^{n}\tilde{P}_{i}$. This alone constituted our observation-based connectivity, allowing for reducing the effect of outliers when incorporating a mixed set of participants and determining a consistent scale. Then the enhanced influence model was computed as in (4). Choosing $\delta=0.095$ we obtained the empirical null distribution using 1000 permutations.

Choosing a confidence level of 95% ($\alpha = 0.05$) and the maximum component size tested K = 10, we found $s^* = 4$, where $s^* = argmin_{h \in 1, ..., K} \mathbb{P}(X_h > \mathbb{E}_{H_0}[X_h]) < \alpha/K$. Table 2 depicts the permutation testing results for different s values and the selection of s^* by its empirical p-value. We are then able to restrict the components that should be individually tested to those of size at least 4, comprising the set $H_s(\delta)$ shown in Table 3. The p-values derived from component-specific testing are quite low, ostensibly due to a high level of consistency across the relatively large sample size.

S	Observed X_s	p-value	$\mathbb{E}_{H_0}[X_s]$
2	17	0.06	12.35
3	5	0.02	1.72
4	4	$< 10^{-4}$	0.32
7	3	$< 10^{-4}$	4×10^{-3}
10	2	$< 10^{-4}$	0

Table 2: Neuro-Hotnet monte carlo results, $\delta = 0.095$.

To better understand the effect of the threshold δ , Figure 7 illustrates the number and sizes of components left in the enhanced influence graph as well as those that are found significant by hypothesis testing. The number of components initially increases with δ as removing the edges with the smallest influence values splits large components. This result is also reflected in the decreasing trend of average size. After a certain δ value, these smaller components do not split into more components but start to shrink, eventually disappearing altogether as the threshold exceeds even the largest edges. When including the significance test sharp jumps emerge in both the count and sizes of components. The jump occurring in both plots at the chosen threshold of $\delta = 0.095$ represents where the larger components considered significant are at their smallest right before being broken up into many smaller components at $\delta \geq 0.1$. Assuming the aim is to identify large components, this approach can be used for selection of the best threshold to reveal the significantly connected regions within these larger components. This approach is similar to selection of number of principal components in principal component analysis or selection of the number of clusters in unsupervised clustering.

$4.2 \quad siGGM$

A similar process was carried out using siGGM with Diffusion. Let \tilde{V} denote the average of 308 participants' sample covariance matrices. The resulting \tilde{V} and $G(\gamma)$ were combined with the GGM framework, yielding the maximum a posteriori log-likelihood estimate of FC across all participants $C(\nu)$ with $\nu=0.011$. All connected components $S(\nu)$ of $C(\nu)$ are shown in Table 3. The choice of the threshold ν is important as a small ν tends to result in fewer but larger components, while a larger value results in numerous pairs and triplets, i.e. ν penalizes inclusion of edges, inducing sparsity and splitting discovered components into smaller groups. Small values of ν result in numerical issues in computation. $\nu=0.011$ was chosen to find components of size at least 10. Second, the component-specific testing phase was implemented similar to the second stage of

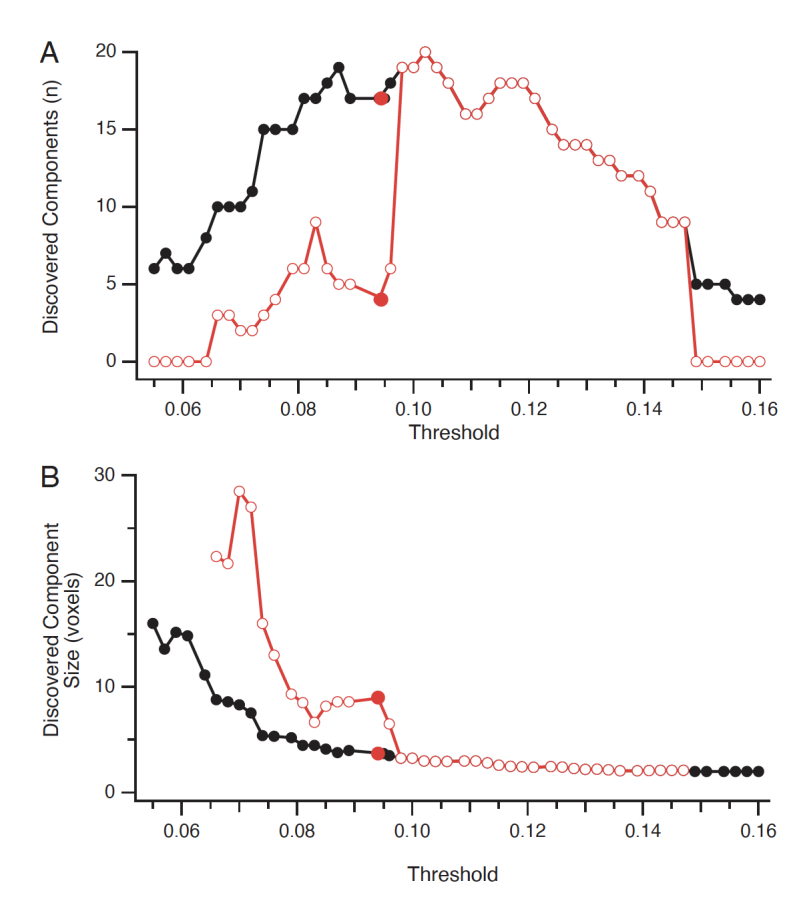


Figure 7: The effect of the threshold δ on the number of connected components and sizes of those components. Both plots feature the effects on the enhanced influence $H(\delta)$ (no hypothesis testing) and Neuro-Hotnet estimates obtained as significant. Marked in red is the point corresponding to the δ value used in the results in Table 3.

the Neuro-Hotnet. The results of the two algorithms agreed almost perfectly (except a single node) on three of the discovered subnetworks. The fourth discovery with siGGM is a subset of the fourth component in Neuro-Hotnet. Without Neuro-Hotnet's testing scheme that prioritizes larger components, siGGM also finds pairs and triplets with high connectivity. These results suggest that this use of siGGM may be better suited to detecting highly significant small components. Similarly, low tract and degree averages as in Neuro-Hotnet are observed for all components, again showing the effectiveness of the influence graph.

To better understand the role of the tuning parameter ν , Figure 8 illustrates how the number of components and their sizes in the maximum a posteriori estimate $C(\nu)$ changes

with ν . In general, similar trends as in Figure 7 may be observed. However, as in Table 3, siGGM tends to discover many pairs that are not identified by Neuro-Hotnet resulting in a decrease of average component size and a sharper drop in the plot representing the component size. Similar to the chosen δ in Neuro-Hotnet this ν resulted in the discovery of the most significant nodes within the larger regions, but any higher values broke these up into numerous pairs and triplets.

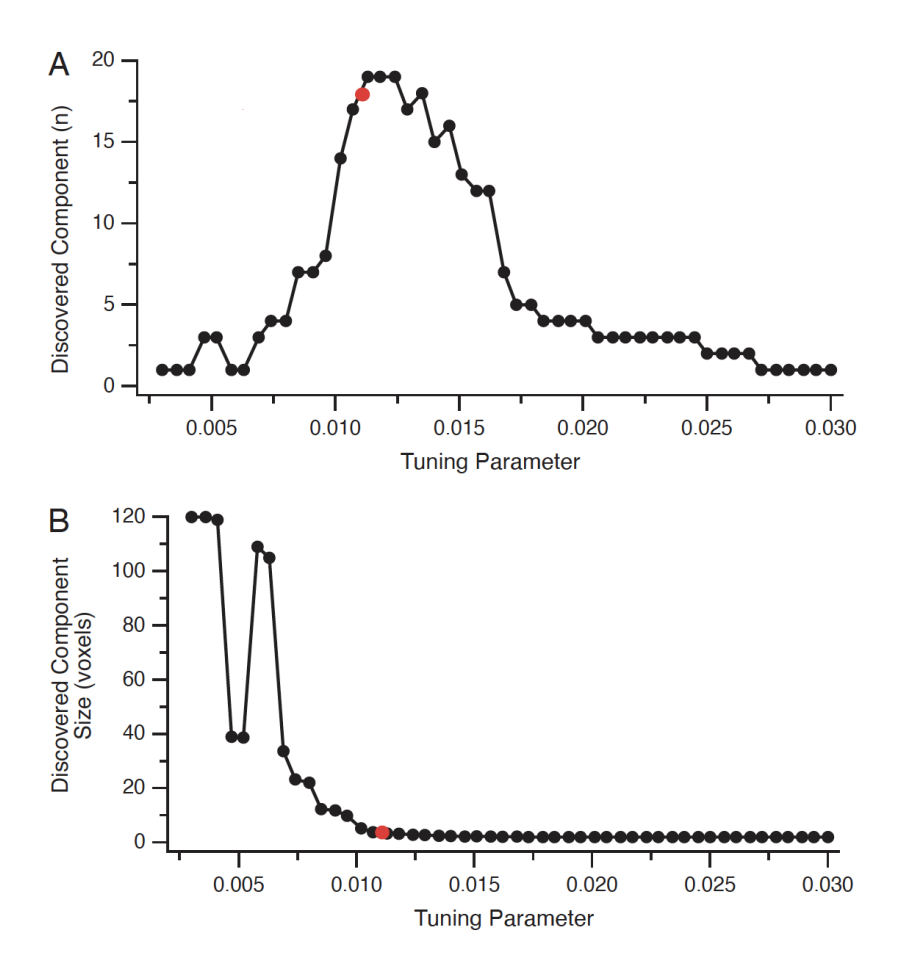


Figure 8: The effect of the tuning parameter ν on the number of connected components and sizes of those components in $C(\nu)$. Marked in red is the point corresponding to the ν value used for the results in Table 3.

4.3 SC Naive methods

Table 3 shows results for the SC naive approach with $\varepsilon = 10^{-60}$. We selected this threshold to yield results of similar size to Neuro-Hotnet and siGGM for ease of com-

parison. The SC naive method partially agrees with the SC informed algorithms on the first component with very high tract and degree averages. The common nodes have high enough correlation in the fMRI data that all three algorithms discover them despite the down-weighting of influence during the diffusion process. This also serves to confirm that Neuro-Hotnet and siGGM can detect a highly correlated cluster in the fMRI data despite the down-weighting of influence. The second component in Table 3 has a tract average twice that (and a significantly higher degree average) of all other results from the SC informed methods. The two most interesting discoveries in the context of motor network FC with low node degrees that the SC informed approaches agree on are not detectable with an SC naive approach.

4.4 Comparison of results

In addition to the superior recovery rates found in Study 1, the SC-informed algorithms leveraging diffusion discover components with the HCP data that the SC naive method misses. Visualizations of the components found with both Neuro-Hotnet and siGGM are presented in Figure 10. Considering the functions of the networks obtained as a result of the proposed algorithms, the results reveal interesting associations between brain regions. For example, one of the subnetworks we obtain using the proposed Neuro-Hotnet approach involves the precentral gyrus, the site of the primary motor cortex, opercular and triangular parts of the inferior frontal gyrus associated with language processing; note that portions of the operculum include the secondary somatosensory cortex, and insula related to awareness, with all these regions occurring in the left hemisphere. The siGGM implementation yields a similar network, though it also includes the postcentral gyrus or primary somatic sensory cortex. Interestingly, the SC naive approach does not include either the precentral or postcentral gyri, which would be expected as part of the findings given the performance of the motor task in this experiment.

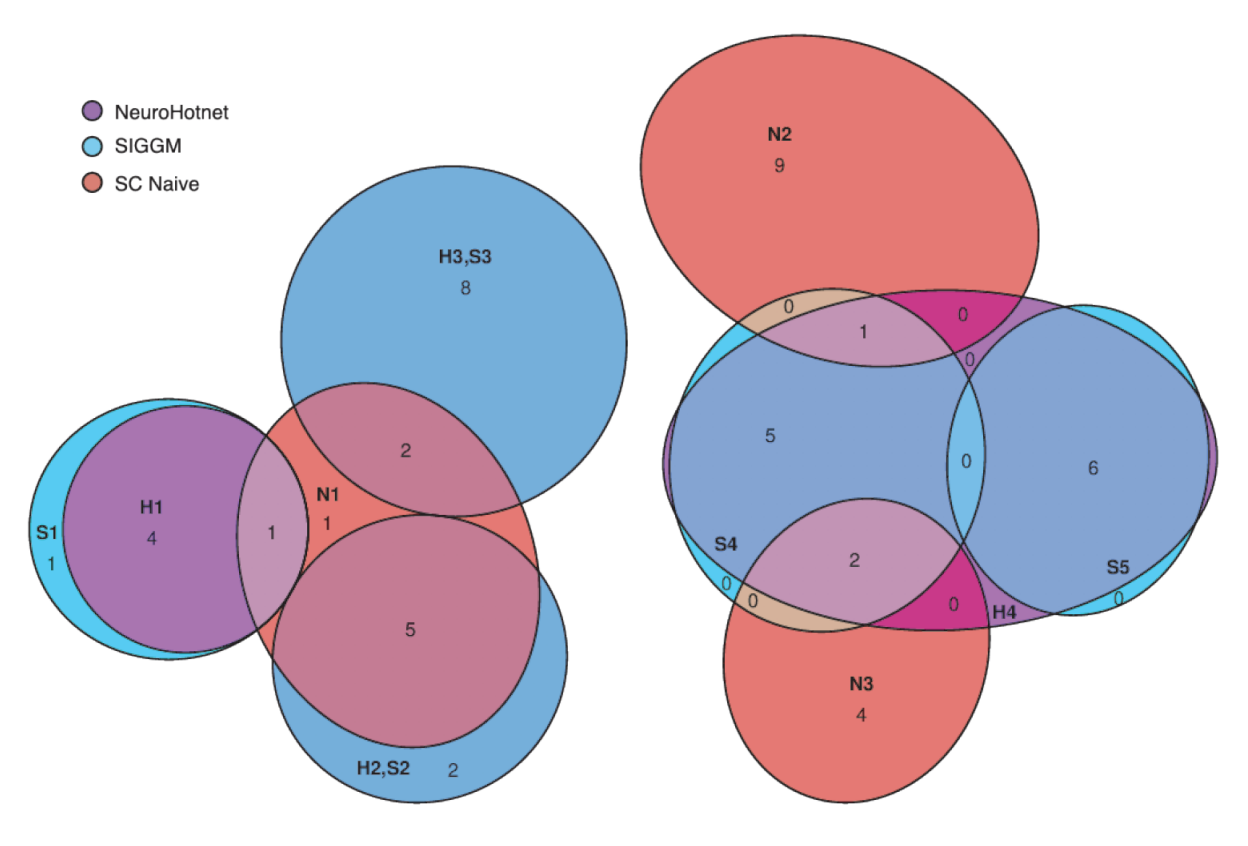


Figure 9: Euler diagram comparing discovered regions in Table 3 of size greater than 3 for all methods. Numbers in overlaps represent the number of regions in common between the components. The blue circles labelled H2,S2 and H3,S3 depict the perfect overlap of the second and third regions for Neuro-Hotnet and siGGM.

	Label	l Size	Regions	p-value	Degree	Density
	H1	5	PreCG.L IFGoperc.L IFGtriang.L	$< 10^{-40}$	8,667	96.6
Neuro			ROL.L INS.L			
Hotnet	H2	7	SFG.L SFG.R MFG.L SMA.L	$< 10^{-69}$	29,412	55.0
$\delta = 0.095$			SMA.R SFGmedial.L SFGmedial.R			
	H3	10	IFGoperc.R IFGtriang.R ROL.R	$< 10^{-21}$	5,646	46.8
			LING.R FFG.R IPG.R SMG.R			
			ANG.R MTG.R ITG.R			
	H4	14	LING.L FFG.L IPG.L SMG.L	0.48	7,703	32.0
			ANG.L STG.L MTG.L ITG.L			
			Crus1.L Crus2.L CB4.L CB6.L CB7.L CB8.L			
	C ₁			10-47	0.000	41 C
	S1	6	PreCG.L IFGoperc.L IFGtriang.L ROL.L INS.L PoCG.L	< 10-41	8,906	41.6
	S2	7	SFG.L SFG.R MFG.L SMA.L	$< 10^{-69}$	29,412	E1 0
siGGM	52	1	SMA.R SFGmedial.L SFGmedial.R	< 10 **	29,412	31.8
$\nu = 0.011$	S3	10	IFGoperc.R IFGtriang.R ROL.R	< 10 ^{−21}	5,646	31.6
		10	LING.R FFG.R IPG.R SMG.R	< 10	0,040	31.0
			ANG.R MTG.R ITG.R			
	S4	8	LING.L FFG.L IPG.L SMG.L	$< 10^{-17}$	6,657	38.1
			ANG.L STG.L MTG.L ITG.L		,	
	S5	6	Crus1.L Crus2.L CB4.L CB6.L	10^{-14}	9,099	45.9
			CB7.L CB8.L			
	-	3	Crus1.R Crus2.R CB6.R	$< 10^{-46}$	12,082	112.1
		2	12 components	-		_
	N1	9	SFG.L SFG.R MFG.L MFG.R IF-	-	24,195	71.8
			Goperc.R IFGtriang.L IFGtriang.R			
$\varepsilon = 10^{-60}$			SFGmedial.L SFGmedial.R			
	N2	10	CAL.L CAL.R CUN.L CUN.R	-	16,330	67.6
			LING.L SOG.L SOG.R MOG.			
	MO	C	MOG.R IOG.L		T 000	60.2
	N3	6	SPG.L SPG.R IPG.L SMG.L PCUN.L PCUN.R	-	5,899	62.3
		2	6 components		_	_
			o components	-		_

Table 3: Discovered regions for both SC informed and the SC naive approach. Label annotates the regions as they are shown in Figure 9. p-values are calculated as in (8) against a mean correlation of 0.5. Degree is the average number of tracts ending in each node (weighted degree) over nodes in a given component. Density is the sum of edge weights within the component divided by $\binom{s}{2}$, where s is the size of the component. The values listed are normalized by the density of the whole graph. It is important to note the degree is weighted using the number of tracts in raw DTI graph, while density is weighted by the estimated FC estimates. Degree reveals the final effect of the diffusion process in selecting for the interesting discoveries, and density shows interconnectedness.

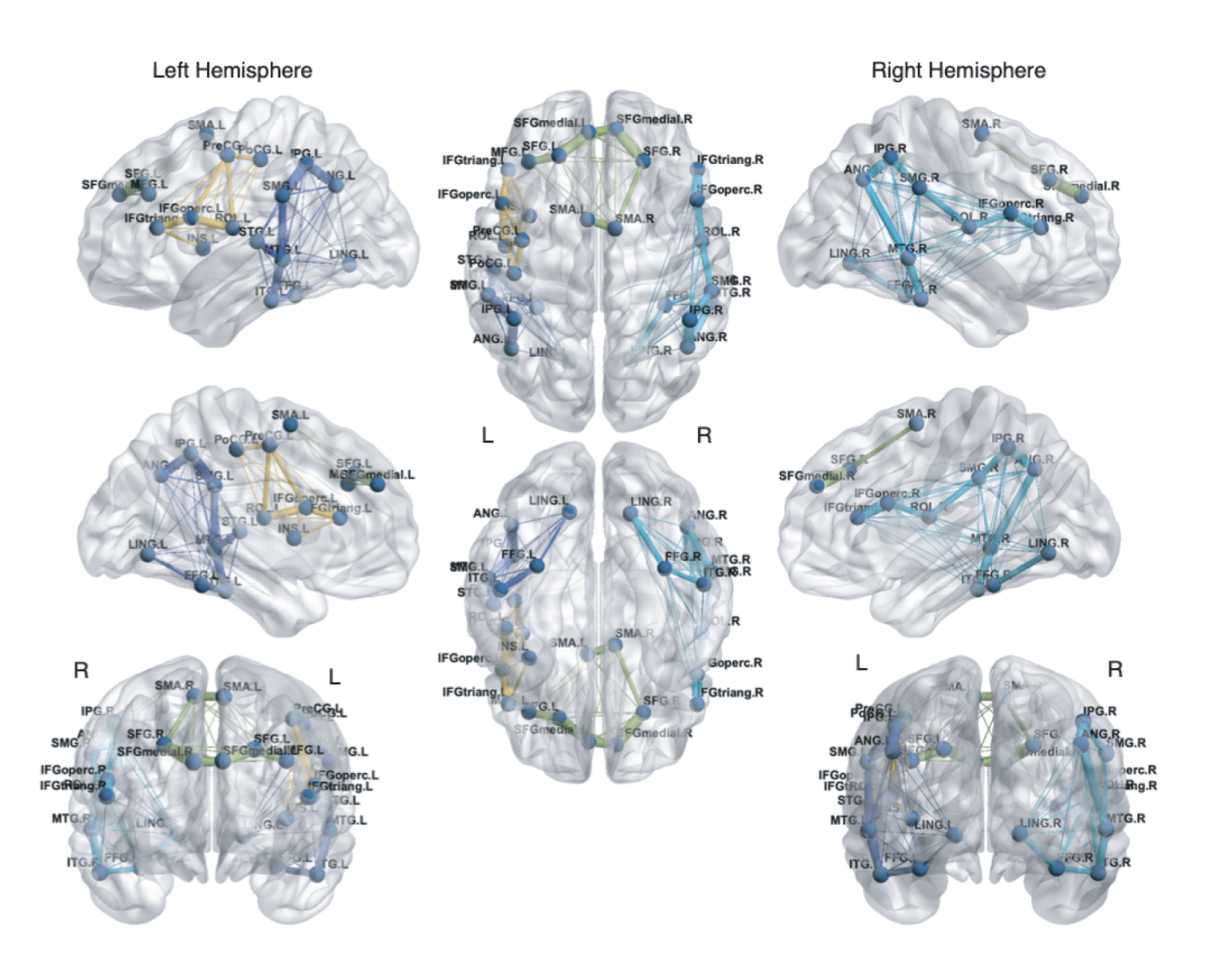


Figure 10: Lateral, Medial, Dorsal, and Ventral views of the 4 components found with both SC informed methods.

5 Discussion

We found that Neuro-Hotnet exhibits comparable power to the best current SC-informed FC estimation algorithms, while still allowing desirable control of the significance level of discoveries. The diffusion process appears extremely promising and also complements existing methods like siGGM well, leading them towards potentially more interesting discoveries. Neuro-Hotnet's biggest advantage relates to its simplicity of implementation and scalability, particularly when compared to other related methods. Through the extremely simple combining of structural/observational data with few parameters and nonparametric hypothesis testing, every step of the process is easily reproducible and transparent. This makes Neuro-Hotnet fast to iterate, and we have confidence that it can adapt to the rapidly changing field of FC estimation given its computational scalability.

In addition to scalability, we showed that our proposed SC-informed approaches result in expected FC estimates given the task performed by study participants. Despite this high performance of Neuro-Hotnet, we believe that additional improvements can occur at every step of its implementation. First, it is worth considering other approaches for aggregating subject-level observations than averaging their cross-regional Pearson correlations. More sophisticated methods for combining data across participants may result in a more biologically meaningful aggregate. An approach to handling BOLD fMRI signals to take advantage of their temporal nature is the sliding-window approach, which could serve as an alternative to raw Pearson correlation computed over time for the full experimental data. Another alternative with less precedent is modeling the activation data over time as a multi-layer graph, where each time-point represents a distinct layer connected to adjacent time-point layers. Pearson correlation can then be used to weight the edges on this graph. This representation allows the use of graphical methods to define observed influence between nodes. It is also possible to combine estimates across participants later in the algorithm, for example by combining the enhanced influence graph $H(\delta)$ or even final FC estimates. This may unfortunately come with significant run time costs depending on

where in the algorithm this aggregation takes place. After fMRI data is aggregated, (4) describes how this aggregate is combined with structural influence to estimate FC. While multiplication is used to combine these values, it is by no means the only or necessarily best function. In addition, either term could be exponentiated prior to multiplication to eliminate negative values and tune how the estimates scale with influence. Different effects could also be achieved by raising either term to a power less than or greater than 1. A strength of Neuro-Hotnet is that its structure allows for relatively easy modifications of the algorithm to incorporate these and other amendments and explore the effects of these changes on the results.

Another promising area for improvement is an analytical approach of choosing the threshold δ . Figure 7 depicts the hand-selected δ , but its positioning directly before the sharpest jumps in both number and size of connected components suggests it could have been selected programmatically similar to the elbow methods used in unsupervised clustering. The problem of selecting a threshold could be reduced to finding the location of the sharp jump. The critical value δ is closely related to the γ used to compute the structural influence graph $G(\gamma)$. γ determines the flow rate of heat during the diffusion process and thus the distribution of influence along the graph. Once incorporated into $H(\delta)$ this changes the relative weights on edges and the δ landscape depicted in Figure 7. Consistently being able to choose δ programmatically would greatly simplify the use of Neuro-Hotnet for diverse datasets and parameter configurations. Future research may develop theoretical considerations for this choice and recommendations on the selection procedure.

Data and code availability

Data used in this project are publicly available for download from the HCP website. All appropriate Data Use Agreements were signed to obtain access to HCP data. We shared

all the code used for simulations and data analyses on GitHub at https://github.com/ntung88/NeuroHotnet.

Acknowledgements

This project was supported by National Institute of General Medical Sciences grant Number 5P20GM103645.

Conflicts of interest

Declarations of interest: none.

References

F. G. Ashby. Statistical analysis of fMRI data. MIT press, 2019.

D. M. Barch, G. C. Burgess, M. P. Harms, S. E. Petersen, B. L. Schlaggar, M. Corbetta, M. F. Glasser, S. Curtiss, S. Dixit, C. Feldt, et al. Function in the human connectome: task-fmri and individual differences in behavior. *Neuroimage*, 80:169–189, 2013.

P. J. Basser, J. Mattiello, and D. LeBihan. Mr diffusion tensor spectroscopy and imaging. Biophysical journal, 66(1):259–267, 1994.

R. L. Buckner, F. M. Krienen, A. Castellanos, J. C. Diaz, and B. T. Yeo. The organization of the human cerebellum estimated by intrinsic functional connectivity. *Journal of neurophysiology*, 106(5):2322–2345, 2011.

E. Bullmore and D. Bassett. Brain graphs: graphical models of the human brain connectome. *Annual review of clinical psychology*, 7:113–140, 2011.

- B. S. Caffo, C. M. Crainiceanu, G. Verduzco, S. Joel, S. H. Mostofsky, S. S. Bassett, and J. J. Pekar. Two-stage decompositions for the analysis of functional connectivity for fmri with application to alzheimer's disease risk. *NeuroImage*, 51(3):1140–1149, 2010.
- M. K. Chung. Brain Network Analysis. Cambridge University Press, 2019.
- B. Efron. Large-scale inference: empirical Bayes methods for estimation, testing, and prediction, volume 1. Cambridge University Press, 2013.
- J. Friedman, T. Hastie, and R. Tibshirani. Sparse inverse covariance estimation with the graphical lasso. *Biostatistics*, 9(3):432–441, 2008.
- I. A. Higgins, S. Kundu, and Y. Guo. Integrative bayesian analysis of brain functional networks incorporating anatomical knowledge. *Neuroimage*, 181:263–278, 2018.
- N. J. Higham. Accuracy and stability of numerical algorithms. SIAM, 2002.
- R. I. Kondor and J. Lafferty. Diffusion kernels on graphs and other discrete structures. In Proceedings of the 19th international conference on machine learning, volume 2002, pages 315–22, 2002.
- J. Lafferty and G. Lebanon. Diffusion kernels on statistical manifolds. *Journal of Machine Learning Research*, 6(Jan):129–163, 2005.
- M. A. Lindquist et al. The statistical analysis of fmri data. *Statistical science*, 23(4): 439–464, 2008.
- X. Ma, H. Lee, L. Wang, and F. Sun. Cgi: a new approach for prioritizing genes by combining gene expression and protein–protein interaction data. *Bioinformatics*, 23 (2):215–221, 2007.
- S. Mori and P. C. Van Zijl. Fiber tracking: principles and strategies—a technical review. NMR in Biomedicine: An International Journal Devoted to the Development and Application of Magnetic Resonance In Vivo, 15(7-8):468–480, 2002.

- W. D. Penny, K. J. Friston, J. T. Ashburner, S. J. Kiebel, and T. E. Nichols. *Statistical parametric mapping: the analysis of functional brain images*. Elsevier, 2011.
- Y. Qi, Y. Suhail, Y.-y. Lin, J. D. Boeke, and J. S. Bader. Finding friends and enemies in an enemies-only network: a graph diffusion kernel for predicting novel genetic interactions and co-complex membership from yeast genetic interactions. *Genome research*, 18(12): 1991–2004, 2008.
- F. Vandin, E. Upfal, and B. J. Raphael. Algorithms for detecting significantly mutated pathways in cancer. *Journal of Computational Biology*, 18(3):507–522, 2011.
- H. Wang et al. Bayesian graphical lasso models and efficient posterior computation. Bayesian Analysis, 7(4):867–886, 2012.
- S. Wang and M. Yuan. Combined hypothesis testing on graphs with applications to gene set enrichment analysis. *Journal of the American Statistical Association*, 114(527): 1320–1338, 2019.
- B. T. Yeo, F. M. Krienen, J. Sepulcre, M. R. Sabuncu, D. Lashkari, M. Hollinshead, J. L. Roffman, J. W. Smoller, L. Zöllei, J. R. Polimeni, et al. The organization of the human cerebral cortex estimated by intrinsic functional connectivity. *Journal of neurophysiology*, 2011.